Pore water chemical constraints on petrophysical shifts following biosilica diagenesis

S. Varkouhi, N.J. Tosca, J.A. Cartwright, Z. Guo, P. Kianoush, A. Jurkowska

Supplementary Information

The Supplementary Information includes:

- Study Site — Geological Setting and Stratigraphy
- Sample Preparation and Analytical Methods
- Tables S-1 to S-2
- Figures S-1 to S-4
- Supplementary Information References

Study Site — Geological Setting and Stratigraphy

Ocean Drilling Program (ODP) Site 794, 40° 11.41′N and 138° 13.86′E, in the northeast of Yamato Basin of the Japan Sea is near the sudden boundary between continental crust of the Yamato Basin and oceanic crust of the Japan Basin (Fig. S-1a). Thus, while basic extrusive compositions are expected, the rock types constituting acoustic basement in the vicinity of Site 794 are diverse. Located ~50 km east of this site is the intensely tectonised zone of the Japan Sea with several thrust and reverse fault complexes of mainly steep dips (Fig. S-1b), some of which concurring with seabed sharp slopes and ridge flanks, and complex folds implicating the Cenozoic deposits (Tamaki and Honza, 1985). About 80 km west of Site 794, over the rifted continental crust near the east of Yamato Rise, normal faults involve the acoustic basement although the structure of basement in the premise of the drilled site is only slightly disrupted by faulting (Shipboard Scientific Party, 1990).

The depositional section encountered at Site 794 comprises 544 m of interbedded hemipelagic silty clay and diatomaceous clay and ooze, with lesser volumes of siliceous clay/claystone and volcanic glass and ash (Fig. 1). The sediment ranges in age from Pleistocene to middle Miocene, and the lowermost Miocene interval overlies a doleritic basement. The section is neither deformed nor disrupted by overburden removal, implying in the context of rather young age of the Yamato Basin (15 Ma; Yoon, 1997) that the back-arc setting subsided to lower–middle bathyal depths through the middle Miocene with dominant deposition of hemipelagic opal-A overburden during the early Pliocene. Mineralogical make-up, fossil content, and sedimentary structures divide the section into five major lithostratigraphic units. The 0–293.5 m interval, with ~55 % of its total volume being biosilica (~54 % diatoms, ~1 % radiolaria, and negligible proportions of siliceous sponge spicules; Alexandrovich, 1992), consists the two upper units I and II (Fig. 1). The last occurrence of opal-A in the sediment at this site coincides with the pronounced formation of opal-CT (α-cristobalite/α-tridymite) (Varkouhi *et al.,* 2020a). This inversion from biosilica toward opal-CT occurs within an opal-A to opal-CT transition zone ($TZ_{A/CT}$) that rests at ~293.5 mbsf, coincident with the lithologic boundary between Subunits IIB and IIIA, and across which notable changes in petrophysical properties are evident (Varkouhi *et al.,* 2020b; Fig. 1). The $TZ_{A/CT}$ exhibits a stratified seismic reflector in the Yamato and northern Japan Basins and lies parallel to the present day seabed, but locally cross cuts the nearby stratal reflections (Fig. S-1c). The upper section of Unit III (Subunits IIIA) hosting the $TZ_{A/CT}$ includes ~58 m of siliceous claystone with interlayers of opal-CT porcellanite and cherts at several levels (Fig. 1). This subunit is differentiated from its overlying diatom clay by a markedly reduced biosilica content, dominant fractions of opal-CT, a denser sediment matrix, and a reduced porosity (Varkouhi *et al.,* 2020a). The highly stratified structure of the seabottom mimicking $TZ_{A/CT}$, also expressed by a corresponding variability in the compressional velocity (Fig. S-1c), indicates significant occurrences of opal-CT porcellanite and chert layers across this diagenetic reaction front (Shipboard Scientific Party, 1990).

Sample Preparation and Analytical Methods

Pore Water Geochemistry

The inorganic chemistry program at Site 794 continued its exclusive focus on analysis of 40 interstitial water samples, from a continuous section between the seabed and 524 mbsf, that were extracted from whole-round cores by Barnes water sampler (BW) and the standard ODP squeezer. The concentration of major cations Ca, K, Li, Mg, Si, Sr, and the primary indicators such as alkalinity, ammonia, chloride, pH, phosphate, salinity, sodium, and sulfate were determined during the shipboard ODP 794 (Shipboard Scientific Party, 1990). A thorough review of the sample preparation and analytical procedures for the pore water from this site is given in Murray *et al.* (1992). Variations in the interstitial water levels of silica and other major ions with burial depth, particularly the concentration gradients near and through the $TZ_{A/CT}$ build a primary source of chemical data for the present study (Fig. S-2).

The saturation index of silica polymorphs involved in biogenic silica diagenesis was assessed utilising the SpecE8 program of Geochemist's Workbench Community. The activity of aqueous silica and saturation status of silica minerals were determined using interstitial water concentrations of dissolved silicon (DSi), major ions (Mg^{2+}, Ca^{2+}, K^+), and primary indicators (pH, Na^+, Cl^-, SO_4^{2-}), and sediment ambient temperatures. This program benefits from the Debye-Hückel theory, which assigns an activity coefficient to each aqueous species using interstitial fluid's ionic strength. Because of the limited precision of this procedure at ionic strengths higher than 1 molal, the SpecE8 calibrates the activity on the basis of actual ionic strength values, whatever is lowest (< 0.5 molal). The program looks through archives of equilibrium constants (from 0 to 300 °C across the steam saturation chart; Bethke and Yeakel, 2016) with which the DSi activity is converted into saturation states with silica polymorphs using the equation:

$$\log (Q/K) = \log Q - \log K \qquad \text{(Eq. S-1)}$$

where Q is the activity of DSi, K the equilibrium constant, and Q/K the saturation index (Fig. 2).

Physical Property Measurements

The ODP performed an inclusive programme of petrophysical measurements on Site 794 core samples, including magnetic susceptibility, Gamma Ray Attenuation Porosity Evaluator density, and compressional wave velocity on the multi-sensor track, index properties, and thermal conductivity. A thorough review of the procedures conducted to collect, analyse, and systematise regular physical properties determinations on recovered sediment samples is given in

Blum (1997). Because of their high resolution measurement intervals (commonly 0.7–1.5 m for density stations, 1–1.5 m for porosity and velocity stations, and ~35 cm for the borehole logging tools; Varkouhi, 2018), physical property data are precise indicators for the depth to anomalous compaction near or at the top of $TZ_{A/CT}$ (*e.g.,* Neagu, 2011). The ODP conducted index properties, including wet-bulk, dry-bulk, and grain densities, porosity, and interstitial water content were utilised in this study to understand the controls on petrophysics of the sediments from Site 794 (Figs. 1–3).

Smear Slides Examination

The relative abundance of biosilica and lithogenic components of Site 794 sediments presented in this study (Figs. 1, 2) is based on the results of smear slides examinations conducted by Varkouhi (2018) and Varkouhi *et al.* (2020a) on 37 core samples provided by International Ocean Discovery Program (IODP). As the core repository was devoid of any sample left from the working-half section, no cored sediment for the first 100 m at this site was at hand for our analyses. Varkouhi (2018) outlines the details of the procedure for preparation of smear slides. During these studies, major and minor compositions of the fine-grained sediments of Site 794 and their biogenic, mineral, and lithogenic fractions were identified and described using smear slides under a polarising Leica optical microscope DM750 P. The volume percentage of these components was estimated by following the visual assessment scheme of Marsaglia *et al.* (2013). For a more accurate identification of lithogenic components as well as the quantification of biosilica, the pre-existing smear slides were further interrogated under the same microscope and photomicrographed in this study (Fig. S-3a–h).

X-ray Diffraction (XRD)

The fine powders prepared from the 37 cores and X-ray diffraction (XRD) scanned by Varkouhi (2018) and Varkouhi *et al.* (2020b) were re-estimated in this work using a PANalytical Empyrean Series 2 powder diffractometer. The methods for preparation of finely powdered samples for XRD analysis are detailed in Varkouhi (2018). The diffractometer with a cobalt source (Co-Ka) having a step rate of 0.0179/s over a 2h range from 5 to 858, housed in the Department of Earth Sciences, University of Oxford determined the abundance and relative extent of opal-CT and major crystalline components of the sediment (Table S-1). Crystalline phases in the samples were identified and quantified using the Match! 3.16 Build 288, which correlates the diffraction pattern of the sample to a reference data source to identify the phases present. The Reference Intensity Ratio (RIR) procedure, built upon scaling the diffraction data of phases in the sample to the diffraction of reference material (corundum), was applied to quantify the components with multiple phases. In this method, the normalised weights of identified phases are added up to 100 wt. % of the crystalline proportion.

Scanning Electron Microscopy (SEM)

The polished blocks formerly prepared from 6 core samples of Site 794 and analysed under scanning electron microscope (SEM) by Varkouhi (2018) and Varkouhi *et al.* (2020a, 2020b) were re-examined in this study using a FEI Quanta 650 FEG (field emission gun) SEM, hosted by the Department of Earth Sciences, University of Oxford. Procedures for preparation of resin impregnated polished blocks for SEM observations are reported in Varkouhi (2018). The SEM instrument was run in a high vacuum mode and equipped with a secondary electron detector, enabling the direct observation of the details of the sediments biosiliceous constituents. The textural features, including the presence and distribution of siliceous frustules in the sediment matrix, their dissolution and redeposition as crystalline silica polymorphs, and the fabric and pore evolution were particularly focused (Fig. S-4a–h).

$\delta^{18}O$ Stable Isotope Analysis and Isotopic Temperatures

From the total of 37 core samples, a subset of 27 representative samples with sufficient opal-CT were derived for $\delta^{18}O$ isotopic analysis. Besides diagenetic silica polymorphs (opal-CT and quartz) but minor to nil biosilica contents (Table S-1, Figs. 1, 2), these samples mostly contain clayey fragments and minor fractions of detrital quartz (Fig. S-3d–h). It was thus imperative to isolate diagenetic silica from these samples to exclude oxygen additions from other mineral phases. This purpose was achieved by following Pisciotto *et al.* (1992) separation procedure, which has no marked effects on the isotopic extent of the isolated opal-CT and quartz, and utilises pyrosulfate fusion and acid treatments to eliminate all minerals excluding diagenetic silica, and sodium hydroxide to dissolve opal-CT from sample fractions containing both opal-CT and quartz. Because this chemical procedure cannot differentiate detrital versus diagenetic quartz, the importance of isotopic uncertainties caused by detrital quartz fractions was assessed using formerly published isotopic data from Site 794 (Pisciotto *et al.,* 1992). Combining this assessment with optical microscopic examinations by the present study, which verify fine detrital quartz scattered in the sample, and mineral composition based on XRD analysis of the bulk powdered sediment, the quartz in our interrogated samples is mainly detrital. Accordingly, the $\delta^{18}O$ values of commonly changing from +2 to +18 ‰, with a reference value of +9.36 ‰ in this range, lie within the silica realms known to largely consist of detrital quartz (Kita and Taguchi, 1986). The ^{18}O isotopic analysis of silica for this study was conducted using an isotope ratio mass spectrometers (IRMS) at Stable Isotope Lab of the Department of Earth Sciences, University of Oxford. Refer to Pisciotto (1981) and Pisciotto *et al.* (1992) for a complete review of the method used to prepare the samples for ^{18}O analysis.

Given that each analysed sample contained opal-CT and quartz, the $\delta^{18}O$ of opal-CT was calculated using the equation:

$$\delta^{18}\text{O opal–CT} = [(\delta^{18}\text{O opal–CT+quartz}) - (\text{wt. \% quartz} \times \delta^{18}\text{O quartz})] \div \text{wt. \% opal–CT} \qquad \text{(Eq. S-2)}$$

with a reference value of +9.36 ‰ for $\delta^{18}O$ quartz of the samples (following Kita and Taguchi, 1986). The results of $\delta^{18}O$ opal-CT analysis reported in parts per thousand (‰) are proportional to Standard Mean Ocean Water (SMOW) (Table S-2), with an average of 0.5 ‰ the contrasts among replicate analyses. The isotopic temperatures of silica formation in the sediments were calculated based on the $\delta^{18}O$ values for opal-CT using the fractionation expression of Kita *et al.* (1985) (Table S-2). This expression relates the temperatures of opal-CT formation to oxygen isotopic compositions of silica transformation using a fractionation index (α) between opal-CT and the pore water (Table S-2), which is defined as:

$$\alpha = (1 + 10^{-3}\ \delta^{18}\text{O opal–CT}) \div (1 + 10^{-3}\ \delta^{18}\text{O pore water}) \qquad \text{(Eq. S-3)}$$

This apparent factor is smaller at lower temperatures of opal-CT precipitation (commonly below 60° C), and the smaller fractionation indices are associated with greater variations in the $\delta^{18}O$ of interstitial water (Kita and Taguchi, 1986). Because of minute isotopic depletion gradients in Site 794 (Varkouhi *et al.,* 2020b), the interstitial water from depths nearmost each opal-CT sample makes minor difference in the computed fractionation factor and opal-CT temperatures. Thus, a mean pore water $\delta^{18}O$ of -4.1 ‰ was accepted to be used in Equation S-3 by following Pisciotto *et al.* (1992).

The oxygen isotope fractionation factor of Kita *et al.* (1985) was preferred over other fractionation expressions, including those from Sharp *et al.* (2016), as it links the oxygen isotopic composition of amorphous silica to pore water within a temperature range (35.4–53.3 °C; Table S-2) comparable to that documented for the diagenetic silica conversion (Varkouhi *et al.,* 2021). The computed fractionation factors for the $TZ_{A/CT}$ frontiers (1.0325 across the $TZ_{A/CT}$ top ~293 mbsf and 1.0292 near the base at 345 mbsf, with $\delta^{18}O$ values of 28.3 and 24.8 ‰, respectively; Table S-2) match those of the moderate to high temperature (> 30°C) expression of Knauth and Epstein (1976) for ODP Site 795 neighbouring Site 794 (1.0286 at the $TZ_{A/CT}$ top 330 mbsf and 1.027 near the $TZ_{A/CT}$ base 405 mbsf; Yanchinila *et al.,* 2020). For both low (< 30 °C) and high temperatures, the fractionation factors in this study, Pisciotto *et al.* (1992), and Yanchinila *et al.* (2020) however markedly differ from those modelled by Ibarra *et al.* (2022) for Site 795 sediments using the Sharp *et al.* (2016) expression. This difference includes the $TZ_{A/CT}$ sediment isotopic temperatures, ranging from 77 to 89 °C (Ibarra *et al.,* 2022), which are more than twice those extracted by Pisciotto *et al.* (1992) for the same sediment. This discrepancy can be related to the thermodynamic state of the $TZ_{A/CT}$ at Site 795 as the isotopic temperatures are typically lower than ambient temperatures across the anomalous compaction interval in that site, while the ancient thermal gradient (233 °C/km) is greater than the present one (132 °C/km; Varkouhi *et al.,* 2020b).

Supplementary Tables

Table S-1 Normalised crystalline contents based on X-ray diffraction analysis of bulk powdered samples in Site 794 (re-analysed and modified from Varkouhi, 2018 and Varkouhi *et al.,* 2020b). α-Crs—α-cristobalite, α-Trd—α-tridymite, An—anorthite, Phg—phengite, Qtz—quartz.

Lithologic unit **	Core, section, interval, cm	Depth, mbsf	Mineral abundance, wt. %					α-Crs, cts
			An	α-Crs	Phg	Qtz	α-Trd	
IIA	127-794A-11H-6, 37–38	100.17	28.3	2.8	29.1	35.6	4.2	402
	127-794A-17X-1, 48–49	149.98	34	5.2	21.7	35.6	3.5	379.7
	127-794A-22X-2, 113–114	200.13	34.3	1.9	24.9	33.6	5.3	472.7
IIB	127-794A-27X-3, 80–81	249.8	36.2	3.5	27.3	28.8	4.2	491.9
	127-794A-31X-4, 100–101 *	290.1	45.8	–	28.4	25.8	–	–
	127-794A-31X-5, 50–51	291.1	35.9	3.1	23.5	33.5	4	486.4
	127-794A-31X-6, 90–91	293	30.4	4.7	23	36.9	5	315
IIIA	127-794A-32X-1, 22–23	293.72	26.9	4.4	26.5	28.2	14	435.7
	127-794A-32X-1, 100–101 *	294.5	37.5	–	25.7	36.8	–	–
	127-794A-32X-2, 5–6	295.05	31	4.7	24	32	8.3	470.1
	127-794A-32X-2, 100–101 *	296	37.3	–	19.3	43.4	–	–
	127-794A-32X-3, 46–47	296.96	30.5	6	23	32.5	8	276.2
	127-794A-32X-3, 100–101 *	297.5	27.5	7	25.2	40.3	–	23
	127-794A-32X-CC, 34–35	298.45	32.3	7.7	23	28	9	263.4
	127-794A-33X-1, 0–1	303.3	1	22.9	15.5	28.6	32	10257.5
	127-794A-33X-1, 5–6	303.35	2	22.5	15.1	30.3	30.1	4257.1
	127-794A-33X-1, 10–11	303.4	1	19.1	19.3	30	30.6	4163.7
	127-794A-33X-1, 35–36	303.65	30.5	6	24	31	8.5	172.7
	127-794A-33X-1, 70–71	304	29.5	5.4	22	30.5	12.6	246
	127-794A-33X-1, 100–101 *	304.3	29	–	29.5	41.5	–	–
	127-794A-33X-1, 104–105	304.34	25.3	5.9	33.5	26.3	9	131.5
	127-794A-33X-2, 9–10	304.89	26.2	6.6	27.3	31.4	8.5	257.5
	127-794A-33X-3, 68–69	306.98	31	6.6	21	33	8.4	288.5
	127-794A-33X-4, 12–13 *	307.92	18.1	24.3	37.7	19.9	–	110
	127-794A-33X-4, 119–120	308.99	29.9	7.5	25	29.8	7.8	217
	127-794A-33X-5, 100–101 *	310.3	33.5	–	20.4	46.1	–	–
	127-794A-33X-6, 20–21	311	27	6.4	27.1	31.1	8.4	264.2
	127-794A-34X-1, 40–41	313	33	7.2	30.1	21.2	8.5	245.2
	127-794A-34X-2, 90–91	315	29	6.5	25.9	31	7.6	295.9
	127-794A-35X-1, 5–6	322.25	28.8	8	23	32	8.2	291.3
	127-794A-35X-2, 30–31	324	28	7.6	24	32	8.4	227.5
	127-794A-35X-3, 80–81	326	30.4	7.6	19.2	34.5	8.3	333.1
	127-794A-35X-4, 130–131	328	28.5	6.1	24.8	33.9	6.7	275

Table S-1 Continued.

Lithologic unit	Core, section, interval, cm	Depth, mbsf	Mineral abundance, wt. %					α-Crs, cts
			An	α-Crs	Phg	Qtz	α-Trd	
	127-794A-35X-6, 38–39	330.08	29.5	7.5	22	32.8	8.2	295
	127-794A-36X-1, 21–22	332.11	29.8	8.2	23.2	27	11.8	149.1
	127-794A-36X-2, 55–56	333.95	28.1	7.7	24.5	31	8.7	316.1
	127-794A-36X-3, 110–111	336	31	7	23.7	30.5	7.8	215.8
IIIA	127-794A-36X-5, 54–55	338.44	31.1	7.3	25.7	24.7	11.2	187.2
	127-794B-5R-1, 39–40 *	338.69	23.6	24.6	16.8	35	–	562
	127-794B-5R-1, 49–50 *	338.79	25	17.2	28.3	29.5	–	317
	127-794A-37X-1, 0–1	341.6	37.4	6	25.6	24.9	6.1	150
	127-794A-37X-2, 19–20	343.29	30.1	6.8	25.5	29.8	7.8	276.5
	127-794A-37X-3, 40–41	345	25.6	7.9	33.6	17.4	15.5	266.1
	127-794A-37X-3, 140–141	346	26.1	17.5	24.5	22.9	9	543.2
	127-794A-37X-CC, 30–31	346.63	28.7	8.8	15	23	24.5	347.5
	127-794B-6R-CC, 5–6	347.85	24.6	11.4	18.3	19.9	25.8	912.7
	127-794B-6R-CC, 7–8 *	347.87	28.9	27.1	19.2	24.8	–	620

* Relative abundance of mineral phases derived from XRD analyses performed by ODP, accessible through IODP (2014).

** Refer to Lithology column of Figure 1 for description of the stratigraphic units.

Table S-2 Opal-CT and quartz contents, normalised to 100 wt. % of the crystalline fraction, and their oxygen isotopic composition and fractionation factors between the silica precipitates and pore water (α) for samples from Sites 794. Also shown are isotopic temperatures derived based on $\delta^{18}O$ of opal-CT and the fractionation factor.

Core, section, interval, cm	**Depth, mbsf**	**Abundance, wt. %**		**$\delta^{18}O$ Qtz + Opal-CT, ‰**	**$\delta^{18}O$ Opal-CT, ‰**	**α**	**Temperature,°C**
		Opal-CT	**Qtz**				
127-794A-31X-5, 50–51	291.1	17.5	82.5	12.8	29.1	1.0333	41.8
127-794A-31X-6, 90–91	293	20.8	79.2	13.3	28.3	1.0325	35.4
127-794A-32X-1, 22–23	293.72	39.7	60.3	15.9	25.8	1.0300	48
127-794A-32X-2, 5–6	295.05	28.9	71.1	14.2	26	1.0302	46.8
127-794A-32X-3, 46–47	296.96	30.1	69.9	13.6	23.6	1.0278	53.1
127-794A-32X-3, 146–147 *	297.96	83.2	16.8	21.6	24.1	1.0283	56
127-794A-32X-CC, 34–35	298.45	37.4	62.6	15.1	24.8	1.0290	51
127-794A-33X-1, 0–1	303.3	65.8	34.2	20	25.5	1.0297	49.5
127-794A-33X-1, 5–6	303.35	63.5	36.5	19.7	25.6	1.0298	49.2
127-794A-33X-1, 10–11	303.4	62.4	37.6	19.5	25.6	1.0298	48.8
127-794A-33X-1, 70–71	304	37.1	62.9	15.4	25.8	1.0300	47.9
127-794A-33X-1, 104–105	304.34	36.2	63.8	15.5	26.2	1.0304	46.1
127-794A-33X-3, 68–69	306.98	31.3	68.7	14.7	26.5	1.0307	44.3
127-794A-33X-4, 119–120	308.99	33.9	66.1	15.1	26.3	1.0305	45.6
127-794A-33X-6, 20–21	311	32.3	67.7	14.9	26.4	1.0306	45.1
127-794A-34X-1, 40–41	313	42.6	57.4	16.7	26.6	1.0308	44
127-794A-34X-2, 90–91	315	31.3	68.7	14.8	26.8	1.0310	42.7
127-794A-35X-1, 5–6	322.25	33.6	66.4	15	26.1	1.0303	46.6
127-794A-35X-2, 30–31	324	33.3	66.7	14.9	26.1	1.0303	46.3
127-794A-35X-3, 80–81	326	31.6	68.4	14.7	26.4	1.0306	44.9
127-794A-35X-4, 130–131	328	27.4	72.6	14	26.3	1.0305	45.5
127-794A-35X-6, 38–39	330.08	32.4	67.6	14.7	25.9	1.0301	47.3
127-794A-36X-2, 55–56	333.95	34.6	65.4	15	25.7	1.0299	48.4
127-794A-36X-3, 110–111	336	32.7	67.3	14.6	25.3	1.0295	50.2
127-794A-36X-5, 54–55	338.44	42.8	57.2	16.5	26	1.0302	47.8
127-794A-37X-1, 54–55 *	342.14	85.1	14.9	21.7	24.4	1.0286	55.7

Table S-2 Continued.

127-794A-37X-3, 40–41	345	57.4	42.6	18.2	24.8	1.0292	53.3
127-794A-37X-3, 140–141	346	53.7	46.3	17.8	25	1.0292	52.6
127-794B-6R-CC, 5–6	347.85	65.2	34.8	19.9	25.6	1.0298	49.1
794B-7R-1, 14–15 *	356.74	84.5	15.5	23.8	25.9	1.0301	47.3
794B-9R-1, 56–57 *	376.56	77	23	23.1	25.3	1.0295	50.8
794B-10R-1, 16–17 *	385.76	88.8	11.2	26.4	27.7	1.0319	38.5

* $\delta^{18}O$ isotopic data derived from Pisciotto *et al.* (1992).

Supplementary Figures

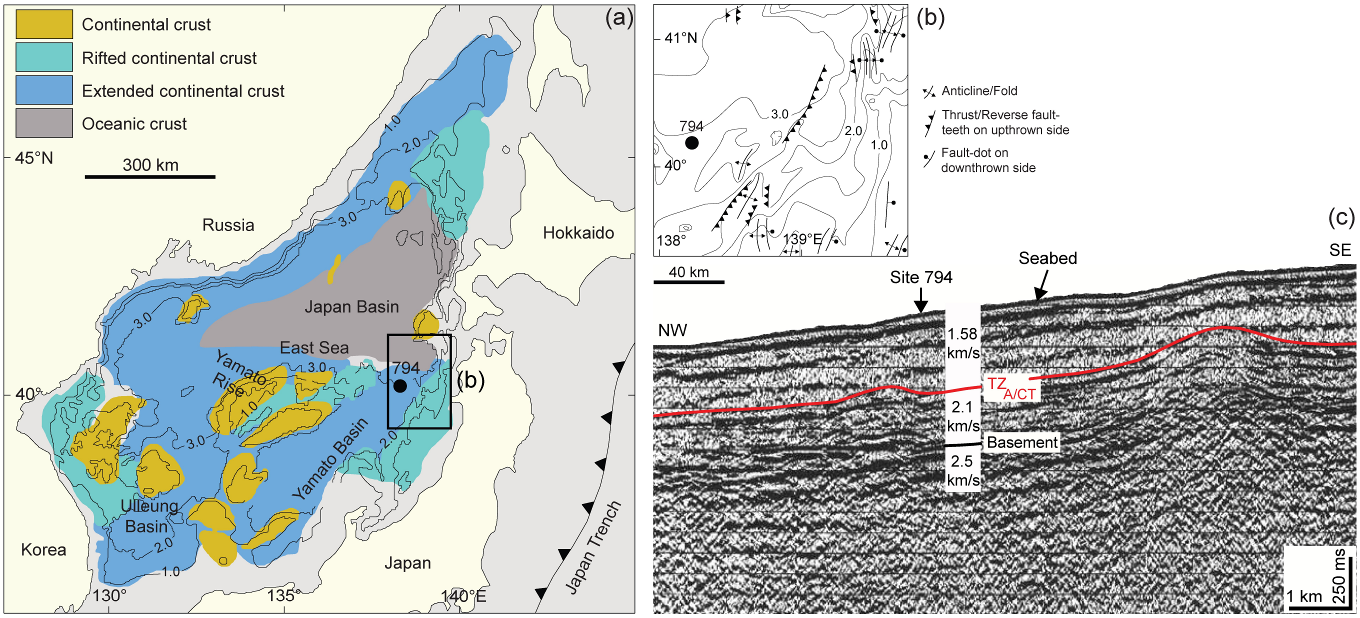

Figure S-1 Tectonic and stratigraphic setting of ODP Site 794. **(a)** Site 794 on map of the Japan Sea crustal structures (redrawn and modified from Tamaki *et al.,* 1992; Yoon *et al.,* 2014). The crust types are differentiated on the basis of seismic surveys, seafloor sampling, geomagnetism, and topographic analyses. Bathymetric contours are in kilometres. **(b)** Site 794 neighbouring highly faulted and folded eastern tectonic zone of the Japan Sea (redrawn and modified from Shipboard Scientific Party, 1990; Varkouhi *et al.,* 2020b). Bathymetric contour lines are in kilometres. **(c)** Opal-A to opal-CT transition zone on a multi-channel seismic section near Site 794 (reprinted and modified from Shipboard Scientific Party, 1990; Varkouhi *et al.,* 2020b). The $TZ_{A/CT}$ cross cuts the host strata, but simulating the modern seabottom.

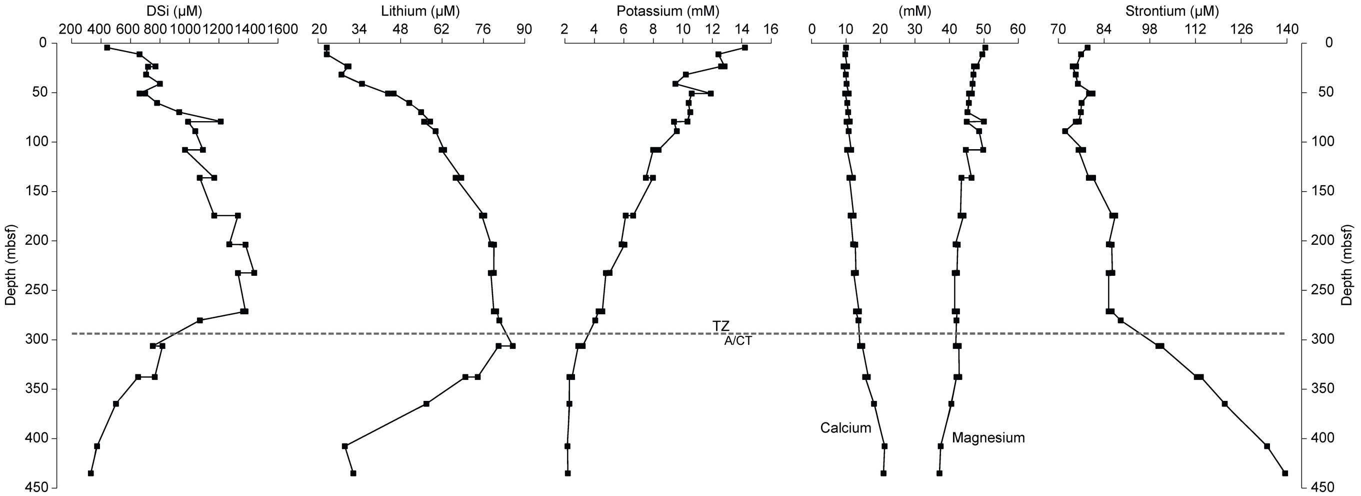

Figure S-2 Concentration–depth profiles of DSi, lithium, potassium, calcium, magnesium, and strontium at Site 794, built upon the data from IODP (2014) open access databank. Dashed line marks the top of the $TZ_{A/CT}$ at ~293.5 mbsf as determined based on abrupt petrophysical changes (Varkouhi *et al.,* 2020a, 2020b).

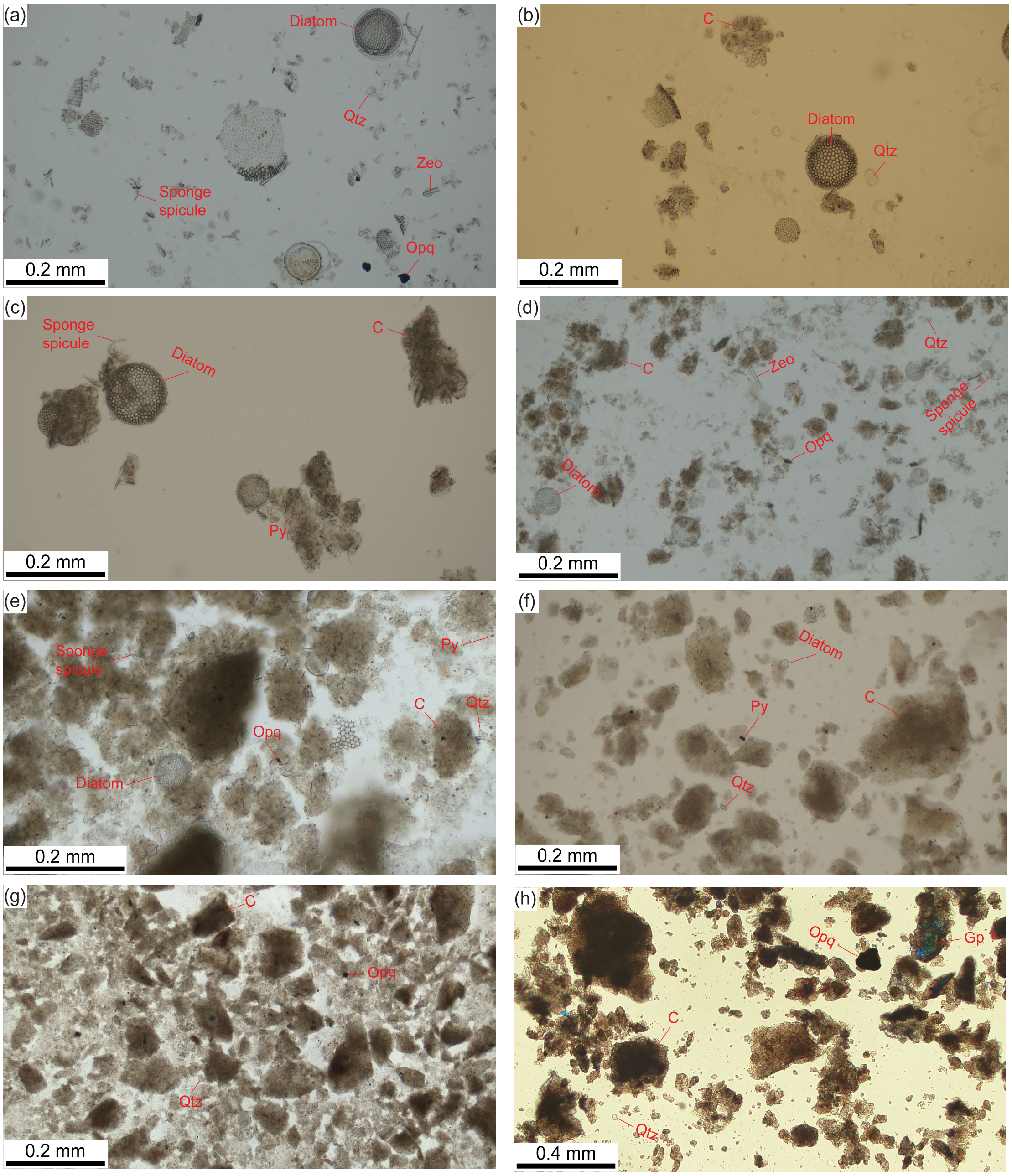

Figure S-3 Photomicrographs of siliceous sediments in Site 794. **(a)** Siliceous ooze with diatoms, low fraction of sponge spicules, and minor quartz, opaque minerals, and zeolite (Sample 127-794A-11H-6, 37–38 cm, at 100.17 mbsf). **(b)** Diatomaceous ooze containing clayey particles and low quartz content (Sample 127-794A-17X-1, 48–49 cm, at 149.98 mbsf). **(c)** Diatomaceous clay with low amount of sponge spicules and minor pyrite (Sample 127-794A-22X-2, 113–114 cm, at 200.13 mbsf). **(d)** Diatom clay containing minor fractions of sponge spicules, quartz, opaque, and zeolite (Sample 127-794A-31X-5, 50–51 cm, at 291.1 mbsf). **(e)** Silty clay with low contents of diatoms and sponge spicules and minor amounts of opaque minerals, pyrite, and quartz (Sample 127-794A-31X-6, 90–91 cm, at 293 mbsf). **(f)** Siliceous clay with minor diatoms, pyrite, and quartz (Sample 127-794A-32X-1, 22–23 cm, at 293.72 mbsf). **(g)** Siliceous claystone containing minor amounts of opaque minerals and quartz (Sample 127-794A-33X-1, 0–1 cm, at 303.3 mbsf). **(h)** Siliceous claystone with opaque minerals and low proportions of quartz and gypsum (Sample 127-794A-37X-3, 40–41 cm, at 345 mbsf). C—clay, Gp—gypsum, Opq—opaque, Py—pyrite, Zeo—zeolite.

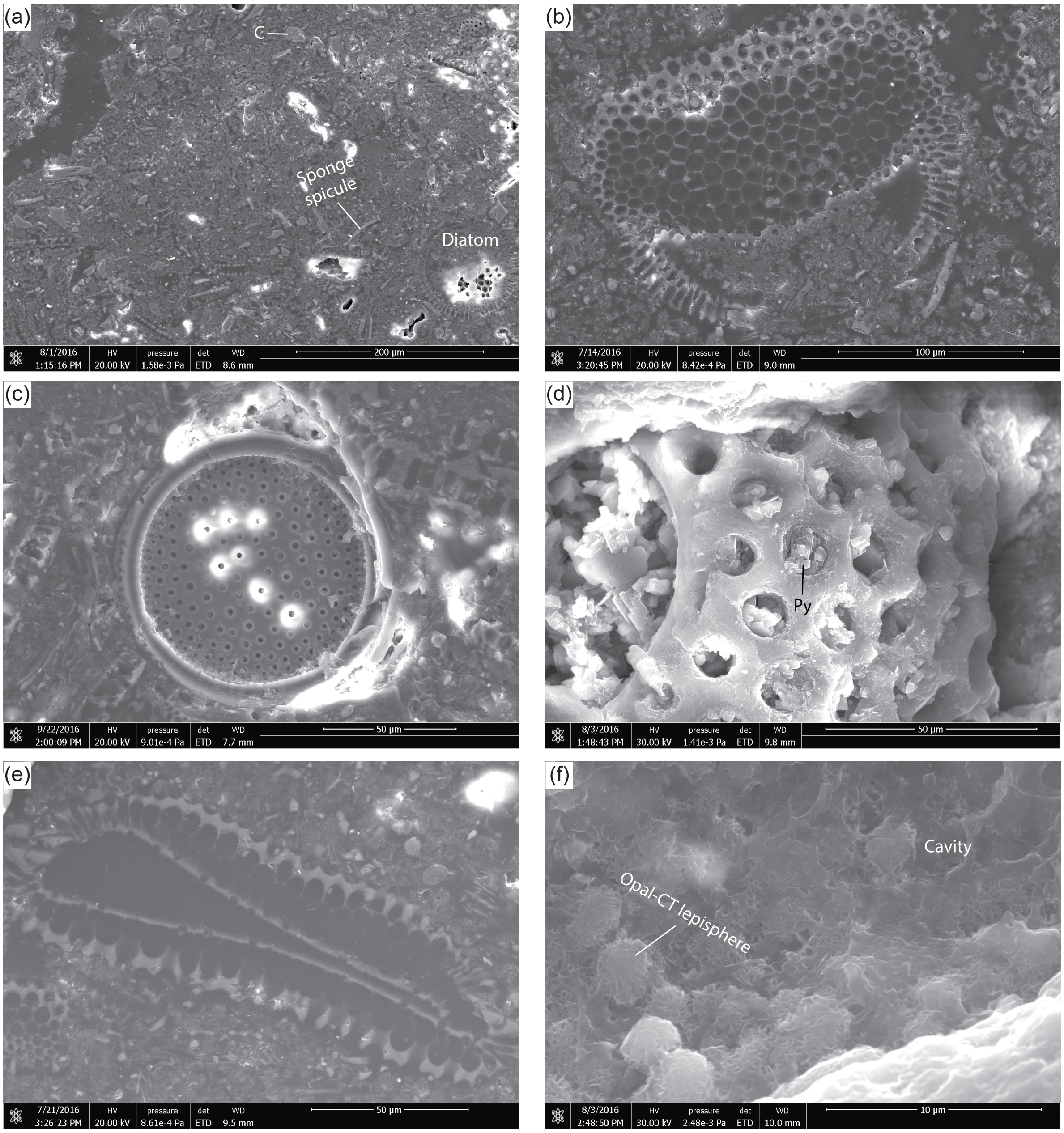

Figure S-4 Scanning electron microscope (SEM) photomicrographs of biosiliceous sediments is Site 794. **(a)** Siliceous ooze with dominant proportion of fragmented and dissolved diatom frustules, clayey particles, and low fraction of sponge spicules (Sample 127-794A-11H-6, 37–38, at 100.17 mbsf). **(b)** Deteriorated outer layer of a diatom valve, and moderate to extensive dissolution of the inner structure starting from the edge of layers (Sample 127-794A-17X-1, 48–49 cm, at 149.98 mbsf). **(c)** Rather intact structure of a diatom valve. This layer survived dissolution but the outer layers were possibly dissolved and removed (Sample 127-794A-17X-1, 48–49 cm, at 149.98 mbsf). **(d)** Authigenic cubic crystals of pyrite filling frustules of a deteriorated diatom (Sample 127-794A-22X-2, 113–114, at 200.13 mbsf). **(e)** Deterioration due to extensive dissolution of a diatom valve (Sample 127-794A-27X-3, 80–81 cm, at 249.8 mbsf). **(f)** Opal-CT lepispheres partly filling a cavity formed from biosilica dissolution (Sample 127-794A-33X-1, 0–1 cm, at 303.3 mbsf).

Figure S-4 Continued.

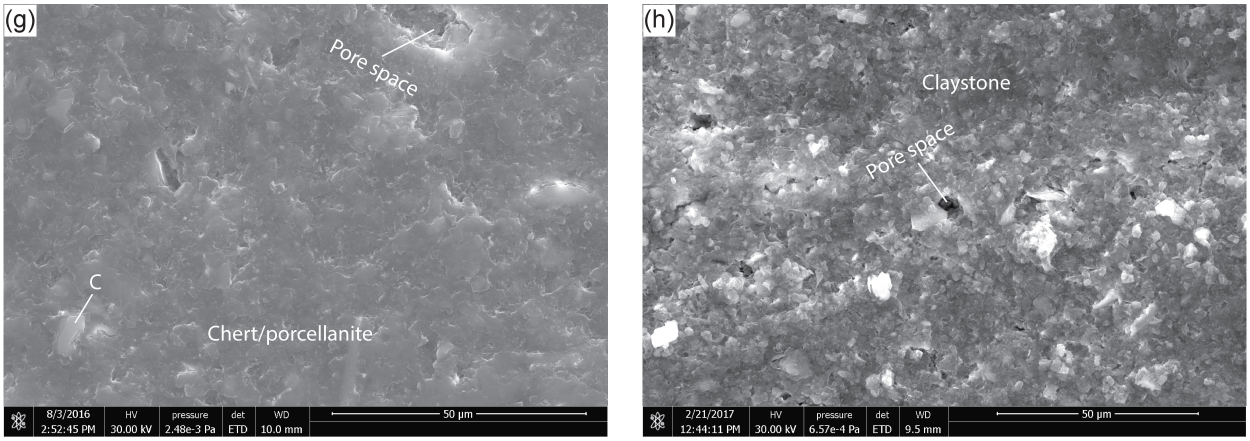

Figure S-4 Continued **(g)** Nearly homogenous dense opal-CT chert/porcellanite facies lacking biosilica (Sample 127-794A-33X-1, 0–1 cm, at 303.3 mbsf). **(h)** Dense claystone with boring-like pores scattered in the sediment matrix (Sample 127-794A-35X-1, 5–6 cm, at 322.25 mbsf).

Supplementary Information References

Alexandrovich, J.M. (1992) Radiolarians from Sites 794, 795, 796, and 797 (Japan Sea). In: Pisciotto, K.A., Ingle, J.C., Jr., von Breymann, M.T., Barron, J., *et al.* (Eds.) *Proceedings of the Ocean Drilling Program. Scientific Results* 127–128 (Pt. 1). Ocean Drilling Program, College Station, Texas, 291–307. http://dx.doi.org/10.2973/odp.proc.sr.127128-1.134.1992

Bethke, C.M., Yeakel, S. (2016) *The Geochemist's Workbench, Release 11: GWB Essentials Guide; Aqueous Solutions LLC*. Champaign, Illinois, 188 p.

Blum, P. (1997) Physical Properties Handbook: A Guide to the Shipboard Measurement of Physical Properties of Deep-sea Cores. *Ocean Drilling Program Technical Note* 26, Ocean Drilling Program, College Station, Texas. https://doi.org/10.2973/odp.tn.26.1997

Ibarra, D.E., Yanchilina, A.G., Lloyd, M.K., Methner, K.A., Chamberlain, C.P., Yam, R., Shemesh, A., Stolper, D.A. (2022) Triple oxygen isotope systematics of diagenetic recrystallization of diatom opal-A to opal-CT to microquartz in deep sea sediments. *Geochimica et Cosmochimica Acta* 320, 304–323. https://doi.org/10.1016/j.gca.2021.11.027

International Ocean Discovery Program (2014) Retrieved from http://web.iodp.tamu.edu/

Kita, I., Taguchi, S., Matsubaya, O. (1985) Oxygen isotope fractionation between amorphous silica and water at 34°-93°C. *Nature* 314, 83–84. https://doi.org/10.1038/314083a0

Kita, I., Taguchi, S. (1986) Oxygen isotopic behaviour of precipitating silica from geothermal water. *Geochemical Journal* 20, 153–157. https://doi.org/10.2343/geochemj.20.153

Knauth, L.P., Epstein, S. (1976) Hydrogen and oxygen isotope ratios in nodular and bedded cherts. *Geochimica et Cosmochimica Acta* 40, 1095–1108. https://doi.org/10.1016/0016-7037(76)90051-X

Marsaglia, K.M., Milliken, K., Doran, L. (2013) Smear Slides of Marine Mud for IODP Core Description: Part I Methodology and Atlas of Siliciclastic and Volcanogenic Components. *International Ocean Discovery Program Technical Note* 1, 263 p. https://doi.org/10.2204/iodp.tn.1.2013

Murray, R.W., Buchholtz ten Brink, M.R., Brumsack, H.-J., Gerlach, D.C., Russ, G.P., III. (1992) Rare Earth, Major, and Trace Element Composition of Leg 127 Sediments. In: Pisciotto, K.A., Ingle, J.C., Jr., von Breymann, M.T., Barron, J., *et al.* (Eds.) *Proceeding of the Ocean Drilling Program*. *Scientific Results* 127–128 (Pt. 1). Ocean Drilling Program, College Station, Texas, 677–695. http://dx.doi.org/10.2973/odp.proc.sr.127128-1.176.1992

Neagu, R.C. (2011) The Relationship between Biogenic Silica Diagenesis and the Physical Properties of Sediments Studied Using Seismic and Well Data. PhD Thesis. Cardiff University, 275 p.

Pisciotto, K.A. (1981) Diagenetic trends in the siliceous facies of the Monterey Shale in the Santa Maria region, California. *Sedimentology* 28, 547–571. https://doi.org/10.1111/j.1365-3091.1981.tb01701.x

Pisciotto, K.A., Murray, R.W., Brumsack, H.J. (1992) Thermal History of Japan Sea Sediments from Isotopic Studies of Diagenetic Silica and Associated Pore Waters. In: Pisciotto, K.A., Ingle, J.C., Jr., von Breymann, M.T., Barron, J., *et al.* (Eds.) *Proceedings of the Ocean Drilling Program. Scientific Results* 127–128 (Pt. 1). Ocean Drilling Program, College Station, Texas, 49–56. https://doi.org/10.2973/odp.proc.sr.127128-1.113.1992

Sharp, Z.D., Gibbons, J.A., Maltsev, O., Atudorei, V., Pack, A., Sengupta, S., Shock, E.L., Knauth, L.P. (2016) A calibration of the triple oxygen isotope fractionation in the SiO_2–H_2O system and applications to natural samples. *Geochimica et Cosmochimica Acta* 186, 105–119, https://doi.org/10.1016/j.gca.2016.04.047

Shipboard Scientific Party (1990) Site 794. In: Tamaki, K., Pisciotto, K., Allan, J., *et al.* (Eds.) *Proceedings of the Ocean Drilling Program. Initial Reports* 127. Ocean Drilling Program, College Station, Texas, 71–167. https://doi.org/10.2973/odp.proc.ir.127.104.1990

Tamaki, K., Honza, E. (1985) Incipient subduction and obduction along the eastern margin of the Japan Sea. *Tectonophysics* 119, 381–406. https://doi.org/10.1016/0040-1951(85)90047-2

Tamaki, K., Suyehiro, K., Allan, J., Ingle Jr., J.C., Pisciotto, K.A. (1992) Tectonic Synthesis and Implications of Japan Sea ODP Drilling. In: Tamaki, K., Suyehiro, K., Allan, J., McWilliams, M., *et al.* (Eds.) *Proceedings of the Ocean Drilling Program. Scientific Results* 127/128 (Pt. 2). Ocean Drilling Program, College Station, Texas, 1333–1348. http://dx.doi.org/10.2973/odp.proc.sr.127128-2.240.1992

Varkouhi, S. (2018) Biogenic Silica Diagenesis under Early Burial in Hemipelagic Marine Sediments. DPhil Thesis. University of Oxford, 428 p.

Varkouhi, S., Cartwright, J.A., Tosca, N.J. (2020a) Anomalous compaction due to silica diagenesis: textural and mineralogical evidence from hemipelagic deep-sea sediments of the Japan Sea. *Marine Geology* 426, 106204. https://doi.org/10.1016/j.margeo.2020.106204

Varkouhi, S., Tosca, N.J., Cartwright, J.A. (2020b) Pore water chemistry — A proxy for tracking the signature of ongoing silica diagenesis. *Journal of Sedimentary Research* 90, 1037–1067. https://doi.org/10.2110/jsr.2020.56

Varkouhi, S., Tosca, N.J., Cartwright, J.A. (2021) Temperature–time relationships and their implications for thermal history and modelling of silica diagenesis in deep-sea sediments. *Marine Geology* 439, 106541. http://dx.doi.org/10.1016/j.margeo.2021.106541

Yanchilina, A.G., Yam, R., Kolodny, Y., Shemesh, A. (2020) From diatom opal-A $\delta^{18}O$ to chert $\delta^{18}O$ in deep sea sediments. *Geochimica et Cosmochimica Acta* 268, 368–382. https://doi.org/10.1016/j.gca.2019.10.018

Yoon, S. (1997) Miocene–Pleistocene volcanism and tectonics in southern Korea and their relationship to the opening of the Japan Sea. *Tectonophysics* 281, 53–70. https://doi.org/10.1016/S0040-1951(97)00158-3

Yoon, S.H., Sohn, Y.K., Choughc, S.K. (2014) Tectonic, sedimentary, and volcanic evolution of a back-arc basin in the East Sea (Sea of Japan). *Marine Geology* 352, 70–88. http://dx.doi.org/10.1016/j.margeo.2014.03.004